

# Proper Orthogonal Decomposition Based Reduced-Order Modeling of Flux-Limited Gray Thermal Radiation

Anthony L. Alberti<sup>a,\*</sup>, Todd S. Palmer<sup>a</sup> and Camille J. Palmer<sup>a</sup>

<sup>a</sup>*Oregon State University, School of Nuclear Science and Engineering, Corvallis, OR, 97330*

---

## ARTICLE INFO

### Keywords:

Reduced-order modeling  
thermal radiation  
shock  
proper orthogonal decomposition  
discrete empirical interpolation method  
principal interval decomposition

## ABSTRACT

In this work, a proper orthogonal decomposition (POD) based reduced-order model (ROM) is developed to solve gray, flux-limited thermal radiation diffusion. We focus on the variable opacity radiation penetration benchmark posed by Olson, Auer, and Hall. The  $T^{-3}$  relationship for opacity in conjunction with high-temperature radiation penetrating an initially cold material produces a strong thermal radiation shock. This class of problems is particularly challenging for standard POD-based reduced-order modeling due to the nonlinearities presented by 1) the  $T^4$  source term, and 2) flux-limited diffusion operator. To address these challenges and develop a cost competitive ROM, we employ a “hyper-reduction” technique through discrete empirical interpolation (DEIM) and allow for adaptive reduced-order projections through principal interval decomposition (PID). Performance of the proposed methodology is quantified by comparing the cost savings and accuracy relative to a full-order computation. Reference solutions and snapshot data are obtained through a full-order calculation performed by the University of Chicago maintained astrophysics code, FLASH. For consistency and potential extensibility, the developed ROM is also implemented in FLASH. We find that in the initialization regime, where the thermal radiation wave is initially created by the warming of the material, this class of problems is highly reducible and suitable for POD-based ROMs. However, the strong convective nature of the wave propagation regime is less reducible and more challenging to create an efficient ROM.

---

## 1. Introduction

Though significant strides have been made in scientific computing in recent years, simulating radiation-hydrodynamics on large computational grids remains challenging. Oftentimes, the computational cost of these problems is driven by the thermal radiation transport component. These equations are inherently complex, nonlinear, and contain seven dimensions. Researchers commonly employ physics-based reductions, often in the form of radiation diffusion, to make the problem more tractable. However, in the presence of sharp gradients or shocks, preserving the fundamental properties of radiation transport is particularly challenging.

Flux-limited diffusion ensures the radiation flux does not exceed the product of the radiation energy density and speed of light. Though it has been shown to reproduce transport-like quality for radiation penetration problems [30], flux-limiting comes at the cost of introducing an additional nonlinearity in the diffusion operator.

To maintain the physical accuracy of flux-limited diffusion while further reducing the computational cost, we investigate the applicability of contemporary proper orthogonal decomposition (POD) techniques for radiation penetration problems. Similar POD-based work has been done in regard to thermal radiation penetration problems for thermal radiation transfer [12, 13, 14, 15], diffusion [23, 32], as well as neutron transport [11, 7, 41, 40, 4, 22]. The novelty of this work lies in applying POD-based methods to flux-limited diffusion. This class of problems is particularly challenging for standard POD-based reduced-order modeling due to the nonlinearities presented by the source term and flux-limited diffusion operator. We address these challenges by utilizing a “hyper-reduction” technique through discrete empirical interpolation (DEIM) [8] and allow for adaptive reduced-order projections through principal interval decomposition (PID) [37].

The remainder of this paper is organized as follows: Section 2 introduces the specific form and discretization technique used to compute the reference solution and snapshots; Section 3 details the POD approaches utilized; Section 4 presents the performance of the developed ROMs; and Section 5 highlights our conclusions and possible follow-on work.

---

✉ [anthony.alberti@oregonstate.edu](mailto:anthony.alberti@oregonstate.edu) (A.L. Alberti)  
ORCID(s): 0000-0003-1609-063X (A.L. Alberti)

## 2. Nonlinear Thermal Radiation in FLASH

In the interest of consistency with the full-order model and extensibility to topics such as (but not limited to) multifrequency, 2D/3D, physics coupling, and tabulated opacities, we use the University of Chicago based astrophysics code, FLASH, as the framework of our reduced-order model (ROM) [20]. To support singular value decomposition, flexible linear algebra, and matrix operations we introduce the scientific libraries, SLEPc and PETSc, to FLASH [25, 38].

Equations 1 and 2 show the specific forms of the gray thermal radiation diffusion and material energy balance equations that are solved in FLASH. Note, 1) the energy of the material (i.e. plasma) is assumed to be determined by its electrons, 2) we omit electron conduction, and 3) the blackbody source emits radiation in a Planck spectrum.

$$\frac{1}{c} \frac{\partial u}{\partial t} - \nabla \cdot \frac{1}{3\sigma(T_e)} \nabla u + \sigma(T_e)u = \sigma a T_e^4 \quad (1)$$

$$\frac{\partial u_e}{\partial t} = \sigma(T_e) [u - a T_e^4], \quad (2)$$

where  $u$  is the radiative flux,  $u_e$  is the electron energy density,  $T_e$  is the electron temperature,  $c$  is the speed of light,  $\sigma(T_e)$  is the total opacity, and  $a$  is the Stefan-Boltzmann constant. As discussed in Section 1, accurately characterizing radiation penetration problems with thermal radiation diffusion requires the use of a flux-limiter on the diffusion coefficient,  $D$ . Recognizing its flaws in reproducing transport-like quality solutions relative to other limiters, we choose to use the ‘‘Harmonic’’ flux limiter (also referred to as the ‘‘sum’’ flux limiter in [30]) for its availability and ease of use within FLASH,

$$D(T_e, u) = \frac{1}{3\sigma(T_e) + \frac{|\nabla u|}{u}}. \quad (3)$$

The nonlinear diffusion operator is discretized using a cell-centered central differencing scheme and the time derivatives are discretized with Implicit Euler. Over each time step,  $n$ , Equation 1 is first solved by assuming that the electron temperature dependent opacity and source are lagged from the previous time step,  $n - 1$ . After discretization, we are left with a ‘‘semi-implicit’’ equation for  $u^n$ ,

$$\frac{1}{c} \frac{u^n - u^{n-1}}{\Delta t} - \nabla \cdot (D(T_e^{n-1}, u^{n-1}) \nabla u^n) + \sigma(T_e^{n-1})u^n = \sigma(T_e^{n-1})a (T_e^{n-1})^4, \quad (4)$$

which can be written in operator form as,

$$\mathbf{A}^{n-1} u^n = u^{n-1} + b(T_e^{n-1}). \quad (5)$$

With  $u^n$  and the lagged electron temperature  $T_e^{n-1}$ , Equation 2 can be solved analytically after discretizing in time,

$$\frac{u_e^n - u_e^{n-1}}{\Delta t} = \sigma(T_e^{n-1}) [u^n - a (T_e^{n-1})^4] \quad (6)$$

which can be written as,

$$u_e^n = u_e^{n-1} + b_{e,\text{abs}}(u^n, T_e^{n-1}) - b_{e,\text{emiss}}(T_e^{n-1}). \quad (7)$$

Algorithm 1 shows the standard FLASH algorithm used to solve the full-order model (FOM).

## 3. Reduced-Order Modeling Approach

In this section, we develop a POD-based ROM for Equations 5 and 7. In Section 3.1 a standard Galerkin based POD ROM for Equation 5 is presented. In Sections 3.2 and 3.3 we improve the derived ROM by utilizing the discrete empirical interpolation method for the efficient computation of the nonlinear terms and adaptive reduced-order projections through principal interval decomposition.

---

**Algorithm 1:** Standard FLASH algorithm for gray thermal radiation diffusion.
 

---

```

1 Set  $u(\mathbf{r}, 0)$  and  $u_e(\mathbf{r}, 0)$ 
2 for  $n = 1$  to  $N_T$  do
3   | compute Equation 5
4   | compute Equation 7
5 end
    
```

---

### 3.1. Galerkin Proper Orthogonal Decomposition

Following the snapshot based approach initially introduced by Sirovich [27], we first construct a database containing the reference solutions for  $u$  over the time-domain,  $t \in [\Delta t, T]$ ,

$$\mathcal{S} = \{u^1, u^2, \dots, u^{N_T}\} \in \mathbb{R}^{N \times N_T}, \quad (8)$$

where  $N$ ,  $N_T$ , and  $u^{1,2,\dots,N_T}$  are the number of unknowns in the FOM spatial discretization, number of time points, and vectors of the solution at time step  $t$ , respectively. Note, we omit the initial condition and only consider time steps 1 to  $N_T$ . Using this database, we can compute a singular value decomposition of  $\mathcal{S}$ ,

$$\mathcal{S} = \mathbf{U} \mathbf{\Sigma} \mathbf{V}^T, \quad (9)$$

where  $\mathbf{U}$ ,  $\mathbf{\Sigma}$ , and  $\mathbf{V}$  represent the left singular modes, singular values, and right singular modes, respectively. A reduced-order approximation of  $\mathcal{S}$  can be constructed by retaining the first  $R$  singular values and corresponding left singular modes that capture the dominant features of the reference solution, ideally,  $R \ll \text{rank}(\mathcal{S})$ .  $R$  is commonly found in the following manner,

$$\kappa > \frac{\sum_{i=1}^R \sigma_i^2}{\sum_{i=1}^{\text{rank}(\mathcal{S})} \sigma_i^2}, \quad (10)$$

where  $\kappa$  is a user-specified tolerance. The numerator of Equation 10 is commonly referred to as the ‘‘energy’’ captured by the POD modes [42, 5]. Taking the first  $R$  columns of  $\mathbf{U}$ , we form the POD basis,

$$\mathbf{\Gamma} = \{\xi_1, \xi_2, \dots, \xi_R\} \in \mathbb{R}^{N \times R}, \quad (11)$$

where  $\xi$  is a left singular mode of  $\mathbf{U}$  and  $\mathbf{\Gamma}$  is referred to as the projection matrix. We now assume that the full-order solution,  $u$ , evolves in the  $R$ -dimensional subspace by writing

$$u \approx \sum_{i=1}^R \xi_i u_{r,i} = \mathbf{\Gamma} u_r, \quad (12)$$

where  $u_{r,i}$  is the  $i$ 'th unknown in the reduced-order solution,  $u_r \in \mathbb{R}^{R \times 1}$ . Inserting Equation 12 into Equation 5 and enforcing a Galerkin projection with  $\mathbf{\Gamma}$ , we obtain a reduced-order system of equations, for  $u_r^n$ ,

$$(\mathbf{\Gamma}^n)^T \mathbf{A}^{n-1} \mathbf{\Gamma}^n u_r^n = (\mathbf{\Gamma}^n)^T \mathbf{\Gamma}^{n-1} u_r^{n-1} + (\mathbf{\Gamma}^n)^T b(T_e^{n-1}). \quad (13)$$

where  $(\mathbf{\Gamma}^n)^T$  is the transpose of the projection matrix at time step,  $n$ . Recognizing that the projection matrix is unitary and that in standard POD the projection matrix is independent of time, we can simplify Equation 13 to

$$\mathbf{A}_r^{n-1} u_r^n = u_r^{n-1} + b_r(T_e^{n-1}). \quad (14)$$

The operator,  $\mathbf{A}_r^{n-1}$ , and source,  $b_r(T_e^{n-1})$ , in Equation 14 are nonlinear functions that require the ROM be ‘‘lifted’’ back to the full-order dimension,  $N$ , on each time step. These present as a performance bottleneck and limit the achievable model order reduction. Table 1 shows the projected cost (via number of theoretical operations per timestep) for setting up and solving the reduced-order radiation energy density equation. The computational savings, measured

**Table 1**

Theoretical number of operations per timestep and cost savings for POD based ROM with and without DEIM treatment for radiation energy density. The full-order dimension is assumed constant and with 100 cells.

R	ROM - no DEIM		ROM - w/ DEIM	
	# Opers (Theory)	Savings	# Opers (Theory)	Savings
5	6.3084E+04	5.444	3.2340E+03	106.195
10	1.2167E+05	2.823	1.2767E+04	26.900
15	1.8625E+05	1.844	2.9850E+04	11.505
25	3.3542E+05	1.024	9.1667E+04	3.747
50	8.4833E+05	0.405	4.6583E+05	0.737
75	1.6113E+06	0.213	1.2788E+06	0.269
100	2.6867E+06	0.128	2.6867E+06	0.128

as the ratio of the number of operations in the FOM to the ROM with and without hyper-reduction on the nonlinear terms, are also shown. The concept of hyper-reduction is addressed in Section 3.2 by utilizing the discrete empirical interpolation method.

Following an analogous treatment for Equation 7, we can obtain a ROM for the material energy balance equation:

$$u_{e,r}^n = u_{e,r}^{n-1} + b_{e,r,abs}(u^n, T_e^{n-1}) + b_{e,r,emiss}(T_e^{n-1}). \quad (15)$$

However, we find it impractical to solve the material energy balance in a reduced form for several reasons. First, due to its locality, solving Equation 7 scales linearly and is therefore significantly cheaper to solve relative to Equation 5. Secondly, in Table 2 we find that with the exception of the most theoretically reducible configurations, projecting the material energy balance can be more costly to evaluate than simply leaving the equation in a full-order state and remapping the radiation energy density to the full-order dimension on each time step. Lastly, the physics of radiation penetration problems result in the total source for Equation 7, i.e., the balance between absorption and emission, to generate a nonlinear function that is particularly difficult to characterize with a snapshot-based reduction. As the wave propagates, this class of problems generates a sharp peak at the wavefront that advects across the spatial domain. This characteristic results in either the requirement of many POD modes or an increase in loss of accuracy due to truncation. Based on the combination of the cost metrics presented in Table 2 and the loss of accuracy due to the projection, we choose to leave the material energy balance in the full-order form and remap the energy density to the full-order state on each time step.

### 3.2. Discrete Empirical Interpolation

The combination of DEIM with POD has been shown in the literature to be an effective hyper-reduction technique to address the dependency of POD-based ROMs on the dimension of the original system,  $N$ , [8, 9, 18, 19]. The DEIM approach approximates a nonlinear function by projecting it onto a subspace that is spanned by a basis of dimension  $\ell$ , where ideally  $\ell \ll N$ . This projection operator is found through a SVD process using snapshots for the nonlinear operator. However, we find that using a singular value based approach to determine the truncation of the projection operator is of little use in practice. This limitation has been recognized in the DEIM literature [44]. For simplicity, we use the following simple a posteriori error estimator presented in [8],

$$\|f - \mathbb{D}f\|_2 \leq \mu \|(\mathbb{I} - \mathbf{\Gamma}\mathbf{\Gamma}^T) f\|_2. \quad (16)$$

In the above,  $\mathbb{D}$  is an oblique projector that has an interpolating property at the select,  $\ell$ , coordinates,  $\mathbb{I}$  is the identity matrix of rank  $N$ , and  $\mu$  is a scaling factor dependent on the projection and interpolation points [19]. In particular, we select DEIM-based projection truncations based on the observations of the behavior of  $\|(\mathbb{I} - \mathbf{\Gamma}\mathbf{\Gamma}^T) f\|_2$ .

To illustrate this in the context of the nonlinear terms presented in Section 3.1, we detail the DEIM treatment for the nonlinear operator,  $\mathbf{A}_r$ , and source,  $b_g(T_e)$ , in Sections 3.2.1 and 3.2.2, respectively.

**Table 2**

Theoretical number of operations per timestep and cost savings for setting up and solving several configurations of the material energy balance equation. 1) FOM with remapping of the radiation energy density; 2) POD based ROM without DEIM; and 3) POD based ROM with DEIM.

R	FOM - w/ $U_r$		ROM - no DEIM		ROM - w/ DEIM	
	# Opers (Theory)	Savings	# Opers (Theory)	Savings	# Opers (Theory)	Savings
5	7.0000E+02	0.429	3.5050E+03	0.0856	5.5000E+01	5.455
10	1.2000E+03	0.250	1.2010E+04	0.0250	2.1000E+02	1.429
15	1.7000E+03	0.176	2.5515E+04	0.0118	4.6500E+02	0.645
25	2.7000E+03	0.111	6.7525E+04	0.0044	1.2750E+03	0.235
50	5.2000E+03	0.058	2.6005E+05	0.0012	5.0500E+03	0.059
75	7.7000E+03	0.039	5.7758E+05	0.0005	1.1325E+04	0.026
100	1.0200E+04	0.029	1.0201E+06	0.0003	2.0100E+04	0.015

### 3.2.1. Nonlinear Loss Operator

A DEIM based approximation of the nonlinear operator,  $\mathbf{A}_r$ , begins by first generating a nonlinear snapshot matrix,

$$S_{nl} = \{ \mathbf{A}(x^1)x^1, \mathbf{A}(x^2)x^2, \dots, \mathbf{A}(x^{N_T})x^{N_T} \} \in \mathbb{R}^{N \times N_T}. \quad (17)$$

Following the truncated SVD approach shown in Equations 9 and 10, we can obtain the nonlinear projection matrix,  $\Gamma_{nl} \in \mathbb{R}^{N \times R_{nl}}$ . Projecting the nonlinear operator to the lower-order subspace can be approximated in the following manner,

$$\mathbf{A}(\Gamma x_r) \Gamma x_r \approx \Gamma_{nl} d_{nl}, \quad (18)$$

where  $d_{nl}$  is the corresponding coefficient vector analogous to  $u_r$  in Equation 12. To determine  $d_{nl}$ , a matrix,  $\mathbf{P}$ , is generated to select particular rows of interest from the overdetermined system in Equation 18,

$$\mathbf{P} = \{ e_i \}, \forall i \in 1, \dots, \ell \quad (19)$$

where  $e_i$  represents the  $i^{\text{th}}$  column of the identity matrix.  $\mathbf{P}$  is typically generated by computing the interpolation indices such that the residual between the input basis vector,  $\xi$ , and its approximation,  $\Gamma d$ , is minimized (Algorithm 2, Line 7) [8].

To determine  $d_{nl}$  from Equation 18, we multiply Equation 18 by  $\mathbf{P}^T$ ,

$$\mathbf{P}^T \mathbf{A}(\Gamma x_r) \Gamma x_r = \mathbf{P}^T \Gamma_{nl} d_{nl}, \quad (20)$$

and solve for  $d_{nl}$ ,

$$d_{nl} = (\mathbf{P}^T \Gamma_{nl})^{-1} \mathbf{P}^T \mathbf{A}(\Gamma x_r) \Gamma x_r. \quad (21)$$

Inserting Equation 21 into Equation 18, we can obtain an approximation for  $\mathbf{A}_r$  that does not depend on the full order system dimension,

$$\mathbf{A}_r = \mathbf{A}(\Gamma x_r) = \underbrace{\Gamma_{nl}^T \Gamma_{nl}}_{R \times R_{nl}} \underbrace{(\mathbf{P}^T \Gamma_{nl})^{-1} \mathbf{P}^T \mathbf{A}(\Gamma x_r) \Gamma}_{R_{nl} \times R}. \quad (22)$$

As written, the term  $\mathbf{P}^T \mathbf{A}(\Gamma x_r)$  suggests that Equation 22 still requires “lifting” to the full order dimension,  $N$ . However, in practice the vector of interpolation indices, as produced by Algorithm 2, determines which columns of  $\mathbf{A}$  need to be updated on each time step. Rather than updating the full  $N \times N$  matrix,  $\mathbf{A}$ , Equation 22 simply requires an  $\ell \times N$  approximation to be updated on each time step. Additionally, the matrix,  $\Gamma_{nl}^T \Gamma_{nl} (\mathbf{P}^T \Gamma_{nl})^{-1}$  is independent of time and can be precomputed.

---

**Algorithm 2:** DEIM algorithm. The notation  $\mathbf{I}_{1,h}$  is for a single column of the identity matrix with a value of 1 at index  $p_h$ . The notation,  $\max\{\}$  follows standard Matlab notation.

---

**Input:** Projection Matrix,  $\mathbf{\Gamma} = \{\xi_1, \xi_2, \xi_k\} \in \mathbb{R}^{j \times k}$

**Output:** DEIM Interpolation Points,  $p = \{p_1, p_2, \dots, p_k\} \in \mathbb{R}^k$

```

1   $[\omega], p_1 = \max\{|\xi_1|\}$ 
2   $e_1 = \mathbf{I}_{1,p_1}$ 
3   $p = [p_1]$ 
4   $\mathbf{P} = [\mathbf{P} e_1]$ 
5   $\mathbf{E} = [\xi_1]$ 
6  for  $h = 2$  to  $k$  do
7      Solve  $(\mathbf{P}^T \mathbf{E}) d = \mathbf{P}^T \xi_h$ 
8       $r = \xi_h - \mathbf{\Gamma} d$ 
9       $[\omega], p_h = \max\{|r|\}$ 
10      $e_h = \mathbf{I}_{1,p_h}$ 
11      $p = [p \ p_h]$ 
12      $\mathbf{P} = [\mathbf{P} \ e_h]$ 
13      $\mathbf{E} = [\mathbf{E} \ \xi_h]$ 
14 end
    
```

---

### 3.2.2. Emission Source

Here we consider DEIM based approximations for the nonlinear function,  $b(T_e^{n-1})$ . As in the previous section, we begin by generating a nonlinear snapshot matrix,

$$\mathbf{S}_{src} = \left\{ b(T_e^1), b(T_e^2), \dots, b(T_e^{N_T}) \right\} \in \mathbb{R}^{N \times N_T}. \quad (23)$$

To project to the reduced-order subspace, we generate a projection matrix based on the truncated left singular modes. Using this matrix,  $\mathbf{\Gamma}_{src} \in \mathbb{R}^{N \times R_{src}}$ , the nonlinear operator is projected to its reduced-order space,

$$b(T_e) = \mathbf{\Gamma}_{src} d_{src}, \quad (24)$$

where  $d_{src}$  contains the coefficients of the projection. As in Section 3.2.1, we determine  $d_{src}$  by generating the DEIM interpolation matrix,  $\mathbf{P}_{src}$ , via Algorithm 2 applied to  $\mathbf{\Gamma}_{src}$ . By multiplying Equation 24 with the transpose of the interpolation matrix,  $\mathbf{P}_{src}$ , we obtain an expression for  $d_{src}$ ,

$$\mathbf{P}_{src}^T b(T_e) = \mathbf{P}_{src}^T \mathbf{\Gamma}_{src} d_{src}, \quad (25)$$

$$d_{src} = (\mathbf{P}_{src}^T \mathbf{\Gamma}_{src})^{-1} \mathbf{P}_{src}^T b(T_e). \quad (26)$$

Inserting the expression for  $d_{src}$  into Equation 24, we obtain a reduced-order approximation for  $b(T_e)$ ,

$$b(T_e) = \underbrace{\mathbf{\Gamma}_{src}}_{N \times R_{src}} \left( \underbrace{\mathbf{P}_{src}^T \mathbf{\Gamma}_{src}}_{R_{src} \times R_{src}} \right)^{-1} \underbrace{\mathbf{P}_{src}^T b(T_e)}_{R_{src} \times 1}. \quad (27)$$

If we insert this approximation into Equation 14, our nonlinear source becomes an  $R \times 1$  function,

$$\mathbf{\Gamma}^T b(T_e) = \underbrace{\mathbf{\Gamma}^T \mathbf{\Gamma}_{src}}_{R \times R_{src}} \left( \underbrace{\mathbf{P}_{src}^T \mathbf{\Gamma}_{src}}_{R_{src} \times R_{src}} \right)^{-1} \underbrace{\mathbf{P}_{src}^T b(T_e)}_{R_{src} \times 1}, \quad (28)$$

we find an expression that exists in the reduced order subspace,  $R$ . As in Equation 22, the term on the left in Equation 28 can be precomputed. Additionally, the product,  $\mathbf{P}_{src}^T b(T_e)$ , is not evaluated on the full dimensional space but rather the indices that generate the matrix,  $\mathbf{P}_{src}$  determine which rows of  $T_e$  to use for the update in  $b(T_e)$ . This results in  $b(T_e)$  being evaluated on a  $R_{src} \times 1$  subspace, where ideally  $R_{src} \ll N$ .

### 3.3. Principal Interval Decomposition

The POD ROM given by Equations 14 and 15 and the DEIM approximations in Equations 22 and 28 is well-suited for parabolic systems. However, when a problem is characterized by advective flow, such as in thermal radiation shocks, the efficacy of standard POD DEIM based approaches is challenged as many modes are required to adequately capture the dynamics of the problem using global bases. Rather than use a single set of global bases, one can separate the problem into distinct time intervals to generate local bases that are applicable over particular time windows [37, 3, 6, 10, 16]. This is the core concept behind principal interval decomposition (PID).

There are two issues with using PID. The first is an increase in storage. Rather than compute a single  $N \times N_T$  SVD and store a single  $N \times R$  projection matrix, PID requires  $\mathcal{W}$  SVDs and the storage of  $\mathcal{W}$ ,  $N \times R_i$  projection matrices where  $i \in (1, \dots, \mathcal{W})$ . The second lies in projecting from the reduced-order subspace of one interval to the next (since each interval can have a varying number of POD modes,  $R$ ). In our application, this additional complexity lies in Equation 13 where the contribution from the previous time step is simplified by recognizing that projection matrix,  $\Gamma$  is unitary and independent of time (thereby reducing to the identity). However, with PID, the latter no longer holds true and the product,  $(\Gamma^n)^T \Gamma^{n-1}$ , must be evaluated to project from one reduced-order subspace to another.

We utilize PID by first separating the radiation penetration problem into two primary physics regimes, 1) the initialization phase and 2) the wave propagation phase. These differentiation of these phases is determined qualitatively by identifying when the dynamics of the problem shift from “heating up” the material (i.e., the incident partial current penetrating the cold material and forming a radiation wave) to the formed radiation wave propagating across the domain. Though there likely exist precise methods to measure this transition, for this work, the delineation was found to occur when the wave reaches  $x = 0.2$  cm.

## 4. Results

To quantify the performance of the proposed ROM for physically realistic problems, we choose to focus on the variable opacity test problem from Olson, Auer, and Hall [30]. Here, the gray opacity varies inversely with the cube of the temperature,  $T^{-3}$ . The density,  $\rho$ , and specific heat,  $C_v$  are both assumed to be constant. The density is equal to 1.0 and the specific heat is that of an ideal gas. The test is initially in equilibrium with a temperature of  $T(x, 0.0) = 0.0562T_b$ , where  $T_b$  is the boundary temperature driving an incident partial current on the slab surface at  $x = 0$ ,

$$u(0, t) = \frac{u(0)}{4} + \frac{D(0)}{2} \frac{\partial u(0)}{\partial x}, \quad (29)$$

where

$$T_b = \left( \frac{u(0)}{a} \right)^{1/4} = 1 \text{ keV}. \quad (30)$$

The opposing boundary condition at  $x = L$  is a vacuum boundary condition,

$$u(L, t) = 0 = \frac{u(L)}{4} - \frac{D(L)}{2} \frac{\partial u(L)}{\partial x}. \quad (31)$$

The FOM is discretized from 0 cm to 1 cm with 100 cells. To aid with the time-step restriction resulting from the semi-implicit time discretization and varying space-time dynamics of the radiation penetration problem, we utilize adaptive time stepping with an initial time step of  $10^{-16}$  sec, a maximum of  $2 \times 10^{-13}$  sec, and 1400 time steps in total. Note, for consistency, the ROMs uses the same timesteps as the FOM. Figure 1 shows the reference full-order solution from FLASH at select time points. We observe the initially cold material subject to the incident boundary radiation, heating up, and generating a thermal radiation shock that propagates across the domain.

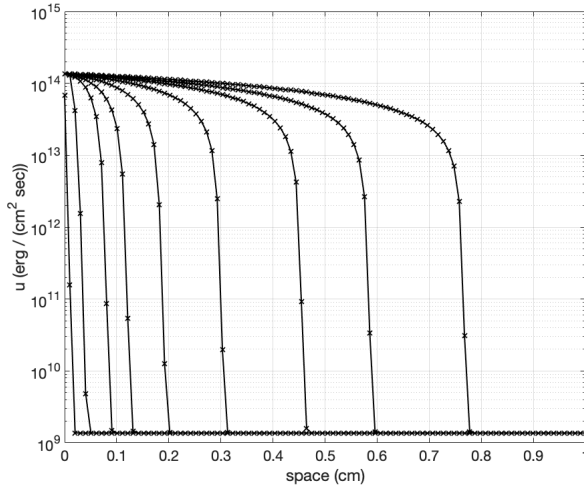


Table 3: Simulation times for data in Figure 1. Data series 1, ..., 9 are for data going from left to right.

Data Series #	Time ( $10^{-12}$ sec)
1	0.00105
2	0.188
3	1.757
4	3.906
5	8.670
6	18.568
7	35.568
8	52.568
9	80.568

Figure 1: Reference full-order solution for Olson radiation penetration problem as select points in time. Legend in Table 3.

To generate the projections for the ROM, we store all 1400 time steps in our various snapshot data sets (ignoring the initial condition). A perceived limitation of this approach is the requirement of solving the full-order system to generate the snapshots. However, POD has been shown to be a viable tool for parameter identification, optimization, and controls. In the context of thermal radiation problems, existing databases of simulation and physical experimental data could be used as snapshot data to generate ROMs. These ROMs could then be used for a variety of topics such as, but not limited to, faster simulations for real-time needs such as predicted energy deposition and temperatures, sensitivity analyses, and parameter identification for future simulations of interest.

We evaluate the performance of the ROMs relative to the FOM by computing a) the absolute relative difference integrated over space as a function of time and b) the computational cost. The absolute relative error is computed as,

$$\epsilon(t) = \int \frac{|\hat{u}(x, t) - u(x, t)|}{u(x, t)} dx, \quad (32)$$

where  $\hat{u}(x, t)$  and  $u(x, t)$  represent the radiative flux for the ROM and FOM, respectively. We also report the maximum and mean value of the absolute relative error over each physics regime. Computational cost is reported for each physics regime and evaluated by profiling appropriate subroutines and averaging over the total number of time steps.

#### 4.1. Without DEIM and PID

To further motivate the use of DEIM and PID, we begin by illustrating the performance of the proposed ROM with standard POD. Due to the convective nature of the radiation penetration problem, the singular value decay of the radiative flux is quite slow - see Appendix A, Figure A-1b. The radiative flux also spans approximately five orders of magnitude, and we find that to sufficiently resolve the wavefront interface, we require at least an SVD truncation of  $10^{-4}$ . If a coarser tolerance is used, we find that the ROM solution at the interface is sufficiently unresolved, becomes unphysical, and eventually unbounded. Based on this requirement and the predictions of Table 1, we expect solutions of sufficient tolerance to be slower than the FOM.

Figure 2 shows both the FOM and several standard POD-based ROM solutions. The underprediction observed from approximately 0.75 to 1.0 cm are present in the early phase of the initialization regime for the ROM with 76 modes and self-resolve as the solution progresses. Figure 3 and Table 4 quantify the performance of the standard POD. Per Figure A-1b, the truncations shown correlate to 76, 78, 79, 81, and 85 modes, respectively. As additional modes are added, particularly beyond a tolerance of  $10^{-6}$ , we observe a stagnation in error, suggesting that the additional cost of adding more modes offers little in terms of accuracy gained in the ROM. As expected, Table 4 shows that the standard POD

**Table 4**

POD-ROM computational cost for varying number of retained POD modes.

SVD Tolerance	$\epsilon(t)$ (max/mean)		Cost (msec/time step)	
	Init.	Wave Prop.	Init.	Wave Prop.
FOM	–	–	0.767	1.669
$10^{-4}$	9.926/1.015	6.722/4.325	5.058	10.303
$10^{-6}$	1.558/0.524	5.892/4.272	5.331	10.872
$10^{-10}$	1.558/0.524	5.892/4.272	5.486	11.101
$10^{-14}$	1.558/0.524	5.892/4.272	5.720	11.610
$10^{-16}$	1.558/0.524	5.892/4.272	6.218	12.698

ROM is significantly slower than the FOM, rendering it useless in practice, and further motivating the use of DEIM and PID.

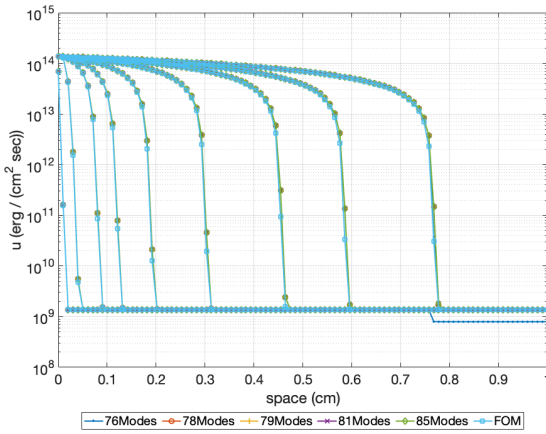


Figure 2: ROM solution with DEIM and PID with reference full-order solution for Olson radiation penetration problem as select points in time. Legend in Table 3.

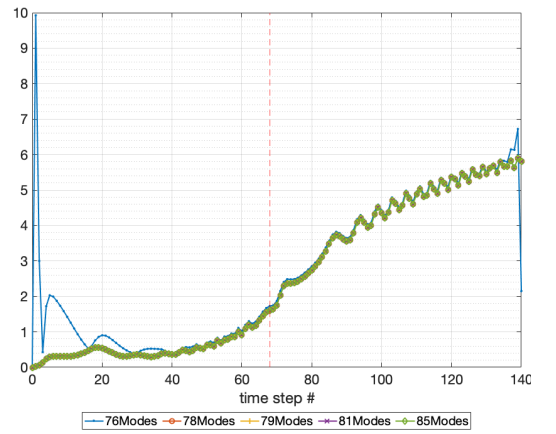


Figure 3:  $\epsilon(t)$  (in %) for ROM without PID and DEIM. Note, the red dashed line indicates the transition from the initialization to wave propagation regime.

#### 4.2. With DEIM and Varying PID

All results in this section include DEIM approximations either with or without PID. “PID1” correlates to the case in which we have a single snapshot matrix for the ROM projection, i.e., equivalent to the results of the previous section with the DEIM modification. We formally introduce PID by first separating the snapshot data into two independent datasets for the two physical regimes; one for the initialization phase and another for the wave propagation phase. This is known as “PID2”. In “PID4” and “PID8”, we simply split each physics regime into two and four additional snapshot matrices, respectively. Figure 4 shows the adaptive time step values used in the FOM and ROMs as well as the bounds for the PID intervals.

To highlight the effects of including the DEIM and PID modifications, we first present results with a fixed truncation of  $10^{-8}$  on each reduced-order operator. As discussed in Sections 3.1 and 3.2, we use the singular value decay to determine the truncation for the radiative flux and the a-priori error indicator, Equation 16, for the truncation of the DEIM operators. In Appendices A and B we show the relevant snapshot and truncation metrics for the “PID1” and “PID2” cases. In the interest of brevity, we choose to not show “PID4” and “PID8” as they are similar in nature.

Figures 5, 6, and 7 show the required number of modes for each reduced-order operator as a function of PID interval. By separating out the physics regimes, we observe that the initialization regime is significantly more reducible than that of the wave propagation regime. This is particularly apparent in Figures 6 and 7 where we have advection in the

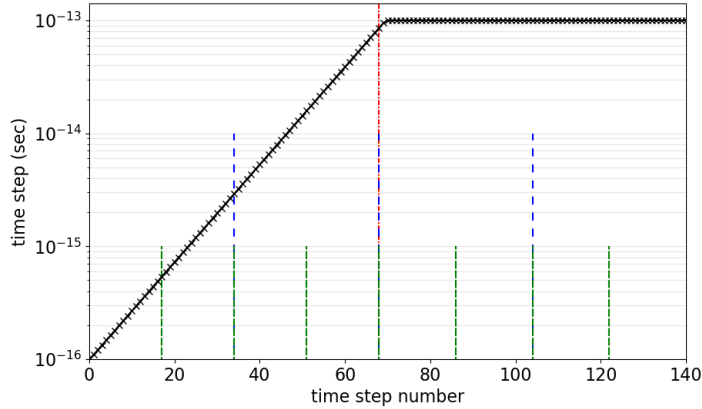
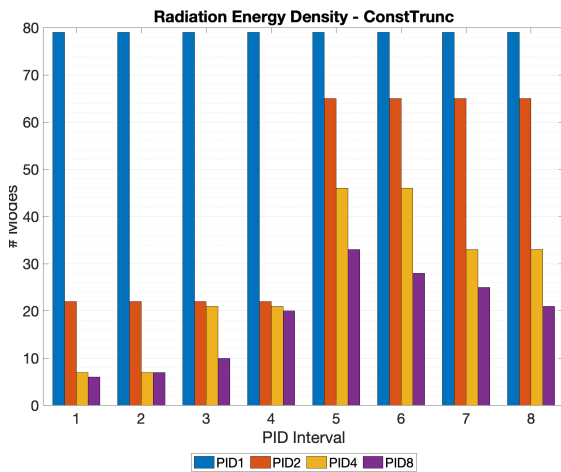


**Figure 4:** Adaptive time step values used in FOM and ROMs. Note, PID interval bounds are represented with the vertical lines. The bounds for each are indicated as follows: red for “PID2”, blue for “PID4”, and green for “PID8”.

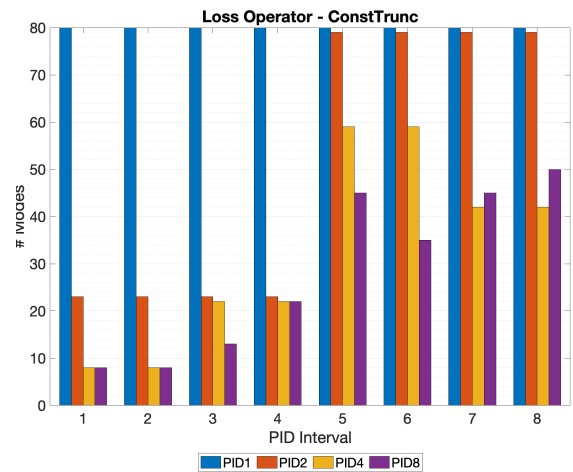
presence of strong nonlinearities. Figure 6 shows the least reducibility due to the strong nonlinear coupling between the flux-limiter and the radiative flux.

Figure 8 shows both the FOM and several POD-DEIM ROM solutions. Relative to Figure 2, we observe a marked improvement in the initialization phase with a degradation in accuracy at the wave front interface of the wave propagation phase for the “PID4” and “PID8” cases. Figure 9 shows the POD-DEIM ROM error as a function of time for the four different PID configurations. We observe that the error increases particularly in the wave propagation region. This is found to be due to nonlinearly propagating error in the truncated radiative flux and DEIM approximated flux-limited loss operator (since the emission term is not as strongly coupled, we find that the accuracy of the ROM is much less sensitive to the truncation in the emission term). We find that the error can be alleviated in a number of ways: 1) eliminate the DEIM approximation, as observed in Section 4.1; or 2) increase the number of retained POD modes in the radiative flux and flux-limited loss operator. We illustrate the effects of the latter in Figures 10 through 13.

Table 5 shows the max and mean of  $\epsilon(t)$  as well as the cost per time step for the initialization and wave propagation regions. Though the cost per time step decreases as we increase the number of PID intervals, we observe an increase in the error due to the discussed nonlinear propagation of error between the radiative flux and flux-limited loss operator.



**Figure 5:** Number of POD modes for radiative flux as function of number of PID intervals with a constant truncation of  $10^{-8}$ .



**Figure 6:** Number of POD modes for flux-limited loss operator as function of number of PID intervals with a constant truncation of  $10^{-8}$ .

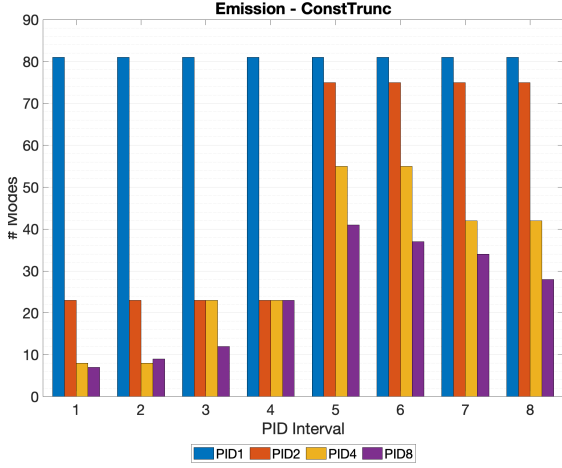


Figure 7: Number of POD modes for emission term as function of number of PID intervals with a constant truncation of  $10^{-8}$ .

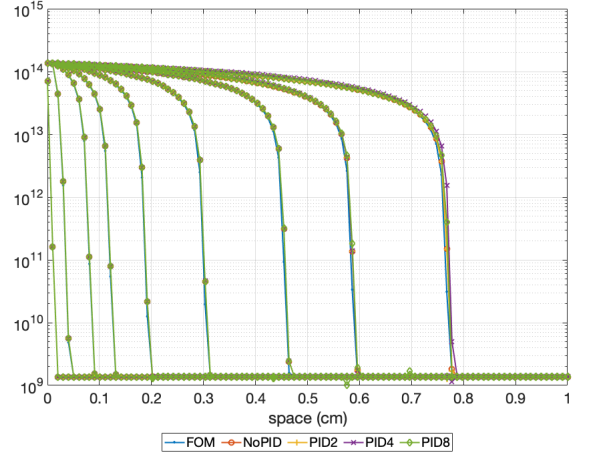


Figure 8: FOM solution with ROM solutions for varying PID intervals each with a constant truncation of  $10^{-8}$ .

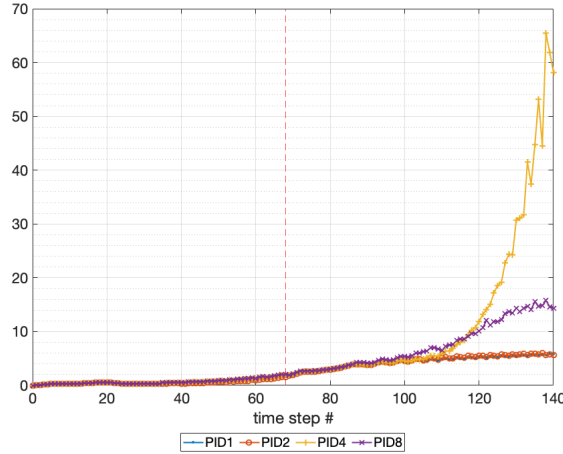


Figure 9:  $\epsilon$  (in %) as a function of time for varying PID intervals with a constant truncation of  $10^{-8}$ .

Table 5: Computational cost and accuracy for the initialization and wave propagation regions for varying PID intervals with a constant truncation of  $10^{-8}$ .

PID Intervals	$\epsilon(t)$ (max/mean)		Cost (msec/time step)	
	Init.	Wave Prop.	Init.	Wave Prop.
FOM	—	—	0.767	1.669
1	1.558/0.524	5.892/4.272	7.013	13.630
2	1.558/0.524	5.991/4.463	0.992	5.559
4	1.935/0.654	65.413/12.584	0.642	1.928
8	2.015/0.682	15.773/7.409	0.584	1.002

To address the nonlinear propagation of error, we increase the number of retained modes in the radiative flux and flux-limited loss operator in an ad-hoc fashion. We observe a decreased sensitivity to the accuracy of the ROM in the

truncation of the emission term and therefore leave it unchanged from Figure 7. Figures 10 and 11 show that to recover the error previously observed, many more POD modes are required. In the case of interval six of “PID8” we need to utilize a nearly full-rank POD approximation. Based on the projection of Table 1, this significantly limits the efficiency of the ROM. However, due to the reductions in the other intervals, we still observe an overall decrease in simulation time as shown in Table 6.

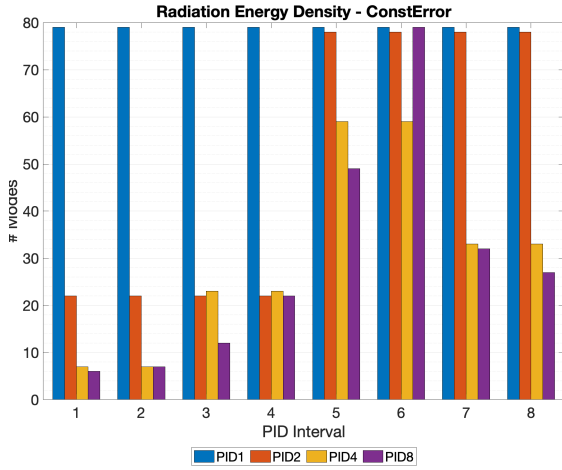


Figure 10: Number of POD modes for radiative flux as function of number of PID intervals while maintaining an equivalent or better error relative to PID1.

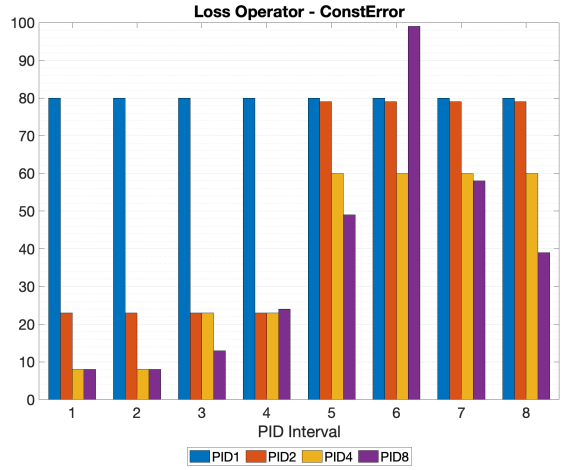


Figure 11: Number of POD modes for flux-limited loss operator as function of number of PID intervals while maintaining an equivalent or better error relative to PID1.

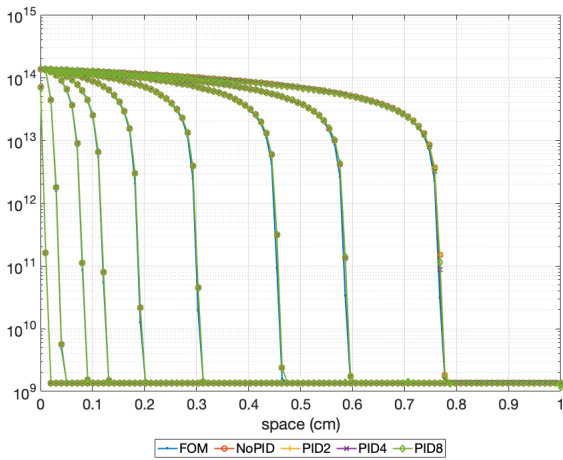


Figure 12: FOM solution with ROM solutions for varying PID intervals each while maintaining an equivalent or better error relative to PID1.

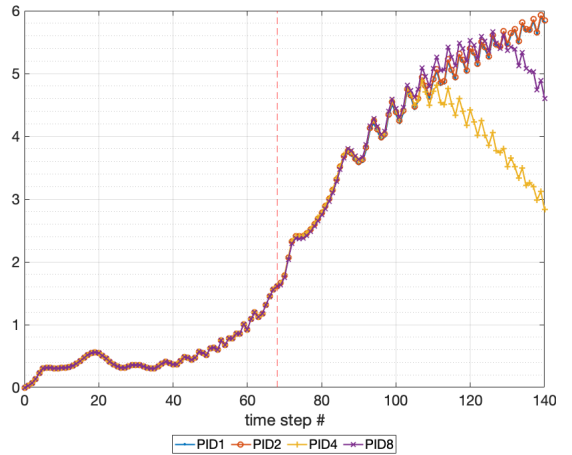


Figure 13:  $\epsilon$  (in %) as a function of time while maintaining an equivalent or better error relative to PID1. Note, reducing the number of modes retained in the final intervals of “PID4” and “PID8” by one results in inaccuracies worse than “PID2”.

Table 6: Computational cost and accuracy for the initialization and wave propagation regions for varying PID intervals while maintaining approximate accuracy of PID1.

PID Intervals	$\epsilon(t)$ (max/mean)		Cost (msec/time step)	
	Init.	Wave Prop.	Init.	Wave Prop.
FOM	–	–	0.767	1.669
1	1.558/0.524	5.892/4.272	7.013	13.630
2	1.558/0.524	5.926/4.307	0.952	7.189
4	1.558/0.524	4.889/3.681	0.665	2.476
8	1.558/0.524	5.665/4.259	0.601	1.114

By utilizing DEIM and PID, we are able to generate ROMs that are competitive to the FOM in accuracy and simulation time. However, in practice, the reduction in simulation time for accurate representations of the reference solution can be limited. We find that this limit can be attributed to three features of the proposed POD-DEIM-PID ROM:

1. Solutions of thermal radiation penetration problems typically span many orders of magnitude [30, 21]. This requires a tight tolerance on the SVD to capture the span of the solution. When combined with the slow decay of advective problems, many singular modes are needed.
2. Flux-limited thermal radiation diffusion involves a strong nonlinear coupling between the radiative flux and flux-limited diffusion coefficient (Equation 3). When using a truncated SVD to generate the POD modes, truncation error propagates nonlinearly between these terms and requires additional modes to yield an accurate ROM.
3. Indicators used for guidance to the truncation of the radiative flux and flux-limited loss operator (i.e., singular value decay and a-priori error estimator) are insufficient in practice due to the nonlinear propagation of error.

The first feature can be addressed by investigating the scaling of both the snapshot data and ROM. Scaling the snapshot data will reduce the span of magnitude and may allow for a coarser tolerance on the truncation. Solving the ROM in the scaled space may also help alleviate the propagation of error and maintain accurate solutions with fewer modes. After being computed, the reduced-order solutions may then be rescaled back to the physical dimension.

Generating effective POD-based ROMs for problems that are characterized by strong advection is currently an open research topic and specific solutions can vary from discipline to discipline. Apart from utilizing PID, other approaches rely on some form of symmetry in the snapshot data, a known wave speed, and an ad-hoc transformation of the reduced-order projections [36, 29]. In [35], Reiss et. al. proposed “shifted POD” and found that with the transport velocity known, a shift operator can be applied to the POD approximation resulting in a significantly faster singular value decay. In theory, this methodology could be applied to the wave propagation regime of radiation penetration problems and result in a much more rapid decay of the singular values and a more effective ROM.

Lastly, recent work has been focused on improving the a-priori error bounds and other performance tuning of standard DEIM. Several separate efforts have been made such as Q-DEIM [18], W-DEIM [19], localized DEIM [31], residual DEIM [45], matrix DEIM [44], and non-negative DEIM [3]. We also recognize alternative approaches for reduced-order projections of neutral particle transport that may be of interest such as dynamic mode decomposition (DMD) [43, 2, 28], operator inference (OPINF) [34, 39], neural nets [26], and non-data driven methods such as proper generalized decomposition [1, 17, 33, 24].

## 5. Future Work and Conclusions

The primary outcome of this work is to illustrate the effectiveness of a POD-based ROM for flux-limited gray thermal radiation diffusion. Temperature dependent opacity, flux-limited radiation penetration problems are particularly challenging for standard POD-based approaches due to 1) the advective nature of the problem, and 2) the strong nonlinearities present in the flux-limited loss operator and source term. To develop a cost-competitive ROM, we employ DEIM approximations on the nonlinear terms as well as adaptive reduced-order projections through PID to account for the advective nature. As discussed in Section 3.1 we find it most effective to project only the radiation energy density equation and leave the material energy balance in its full-order form. Though we are able to generate

ROMs that are accurate and cheaper to evaluate relative to the FOM, we find that the efficacy of our model is limited by the span of the magnitude of the snapshot data and the nonlinear propagation of error between the radiative flux and flux-limited loss operator. Future work should focus on scaling the snapshot data and ROM and improving the truncation properties of the wave propagation regime. This scaled approach should enable lower-order projections while maintaining accurate reduced-order solutions that limit the nonlinear propagation of error between radiative flux and flux-limiter. Additionally, an investigation of the efficacy of the POD-based ROMs presented in this work for parameterized radiation penetration problems, particularly for ROMs evaluated outside of their snapshot data, would be welcome.

### Acknowledgements

The authors would like to thank Dmitry Anistratov and Joe Coale from North Carolina State University for their regular discussions on POD-based ROMs for thermal radiation transfer. We would also like to thank Boris Kramer from the University of California, San Diego for his discussions in regard to DEIM and PID. Each of these contributions were critical to the development of the ROMs shown.

The project or effort depicted in this paper is sponsored in part by the U.S. Department of Defense, Defense Threat Reduction Agency, grant number HDTRA1-18-0042. The content of the information does not necessarily reflect the position or the policy of the federal government, and no official endorsement should be inferred.

The software used in this work was in part developed by the DOE NNSA-ASC OASCR Flash Center at the University of Chicago.

### References

- [1] Alberti, A.L., Palmer, T.S., 2020. Reduced-Order Modeling of Nuclear Reactor Kinetics Using Proper Generalized Decomposition. *Nuclear Science and Engineering* 194, 837–858.
- [2] Alla, A., Kutz, J.N., 2017. Nonlinear Model Order Reduction via Dynamic Mode Decomposition. *SIAM Journal on Scientific Computing* 39, B778–B796.
- [3] Amsallem, D., Nordström, J., 2016. Energy Stable Model Reduction of Neurons by Nonnegative Discrete Empirical Interpolation. *SIAM Journal on Scientific Computing* 38, B297–B326.
- [4] Behne, P.A., Ragusa, J.C., Morel, J.E., 2019. Model Order Reduction For Sn Radiation Transport, in: M&C, Portland, OR.
- [5] Benner, P., Gugercin, S., Willcox, K., 2015. A Survey of Projection-Based Model Reduction Methods for Parametric Dynamical Systems. *SIAM Review* 57, 483–531.
- [6] Borggaard, J., Hay, A., Pelletier, D., 2007. Interval-based reduced-order models for unsteady fluid flow. *International Journal of Numerical Analysis and Modeling* 4, 353–367.
- [7] Buchan, A.G., Pain, C.C., Fang, F., Navon, I.M., 2010. A POD reduced order model for eigenvalue problems with application to Reactor Physics. *International Journal for Numerical Methods in Engineering* , 39.
- [8] Chaturantabut, S., Sorensen, D.C., 2010. Nonlinear Model Reduction via Discrete Empirical Interpolation. *SIAM Journal on Scientific Computing* 32, 2737–2764.
- [9] Chaturantabut, S., Sorensen, D.C., 2012. A State Space Error Estimate for POD-DEIM Nonlinear Model Reduction. *SIAM Journal on Numerical Analysis* 50, 46–63.
- [10] Cheung, S.W., Choi, Y., Copeland, D.M., Huynh, K., 2022. Local Lagrangian reduced-order modeling for Rayleigh-Taylor instability by solution manifold decomposition. *arXiv:2201.07335 [cs, math]* [arXiv:2201.07335](https://arxiv.org/abs/2201.07335).
- [11] Choi, Y., Brown, P., Arrighi, W., Anderson, R., Huynh, K., 2021. Space–time reduced order model for large-scale linear dynamical systems with application to Boltzmann transport problems. *Journal of Computational Physics* 424, 109845.
- [12] Coale, J., Anistratov, D., 2019a. Data-Driven Grey Reduced-Order Model for Thermal Radiative Transfer Problems Based on Low-Order Quasidiffusion Equations and Proper Orthogonal Decomposition, in: *Transactions of the American Nuclear Society - Volume 121, ANS*. pp. 836–839.
- [13] Coale, J., Anistratov, D.Y., 2019b. A Reduced-Order Model for Thermal Radiative Transfer Problems Based on Multilevel Quasidiffusion Method, in: *In: Proc. of Int. Conf. on Mathematics and Computational Methods Applied to Nuclear Science and Engineering (M&C 2019)*, ANS, Portland, OR. p. 10.
- [14] Coale, J.M., Anistratov, D.Y., 2021a. Reduced order models for nonlinear radiative transfer based on moment equations and POD/DMD of Eddington tensor. *arXiv:2107.09174 [cs, math]* [arXiv:2107.09174](https://arxiv.org/abs/2107.09174).
- [15] Coale, J.M., Anistratov, D.Y., 2021b. Reduced-Order Models for Thermal Radiative Transfer Based on POD-Galerkin Method and Low-Order Quasidiffusion Equations, in: *Proc. of Int. Conf. on Mathematics and Computational Methods Applied to Nuclear Science and Engineering (M&C 2021)*, Raleigh, NC.
- [16] Copeland, D.M., Cheung, S.W., Huynh, K., Choi, Y., 2022. Reduced order models for Lagrangian hydrodynamics. *Computer Methods in Applied Mechanics and Engineering* 388, 114259.
- [17] Dominesty, K.A., Ji, W., 2022. Reduced-order modeling of neutron transport separated in energy by Proper Generalized Decomposition with applications to nuclear reactor physics. *Journal of Computational Physics* 449, 110744.
- [18] Drmač, Z., Gugercin, S., 2016. A New Selection Operator for the Discrete Empirical Interpolation Method—Improved A Priori Error Bound and Extensions. *SIAM Journal on Scientific Computing* 38, A631–A648.

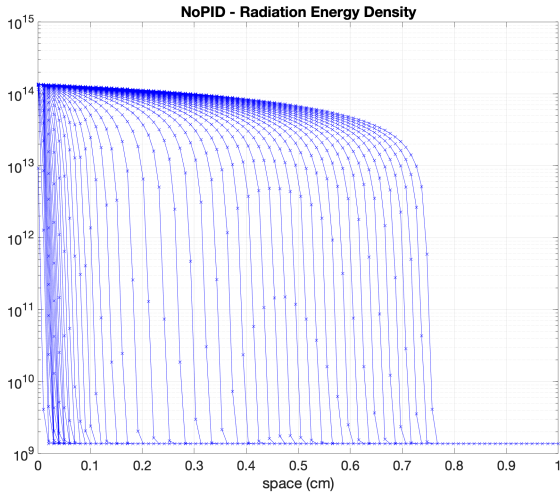
- [19] Drmač, Z., Saibaba, A.K., 2018. The Discrete Empirical Interpolation Method: Canonical Structure and Formulation in Weighted Inner Product Spaces. *SIAM Journal on Matrix Analysis and Applications* 39, 1152–1180.
- [20] FLASH, 2019. FLASH Users Guide.
- [21] Fleck, J., Cummings, J., 1971. An implicit Monte Carlo scheme for calculating time and frequency dependent nonlinear radiation transport. *Journal of Computational Physics* 8, 313–342.
- [22] German, P., Ragusa, J.C., 2019. Reduced-order modeling of parameterized multi-group diffusion k-eigenvalue problems. *Annals of Nuclear Energy* 134, 144–157.
- [23] Girault, M., Liu, Y., Billaud, Y., Benselama, A.M., Saury, D., Lemonnier, D., 2021. Reduced Order Models for conduction and radiation inside semi-transparent media via the Modal Identification Method. *International Journal of Heat and Mass Transfer* 168, 120598.
- [24] González-Pintor, S., Ginestar, D., Verdú, G., 2013. Using proper generalized decomposition to compute the dominant mode of a nuclear reactor. *Mathematical and Computer Modelling* 57, 1807–1815.
- [25] Hernandez, V., Roman, J.E., Vidal, V., 2005. SLEPc: A scalable and flexible toolkit for the solution of eigenvalue problems. *ACM Transactions on Mathematical Software* 31, 351–362.
- [26] Kim, Y., Choi, Y., Widemann, D., Zohdi, T., 2022. A fast and accurate physics-informed neural network reduced order model with shallow masked autoencoder. *Journal of Computational Physics* 451, 110841.
- [27] Lawrence Sirovich, 1987. Turbulence and the Dynamics of Coherent Structures Part 1: Coherent Structures. *Quarterly of Applied Mathematics* 14, 561–571.
- [28] McClarren, R.G., 2019. Calculating Time Eigenvalues of the Neutron Transport Equation with Dynamic Mode Decomposition. *Nuclear Science and Engineering* 193, 854–867.
- [29] Nicolini, J.L., Teixeira, F.L., 2021. Reduced-Order Modeling of Advection-Dominated Kinetic Plasma Problems by Shifted Proper Orthogonal Decomposition. *IEEE Transactions on Plasma Science* 49, 3689–3699.
- [30] Olson, G.L., Auer, L.H., Hall, M.L., 2000. Diffusion, P1, and other approximate forms of radiation transport. *Journal of Quantitative Spectroscopy and Radiative Transfer* 64, 619–634.
- [31] Peherstorfer, B., Butnaru, D., Willcox, K., Bungartz, H.J., 2014. Localized Discrete Empirical Interpolation Method. *SIAM Journal on Scientific Computing* 36, A168–A192.
- [32] Pinnau, R., Schulze, A., 2007. Model reduction techniques for frequency averaging in radiative heat transfer. *Journal of Computational Physics* 226, 712–731.
- [33] Prince, Z.M., Ragusa, J.C., 2020. Application of proper generalized decomposition to multigroup neutron diffusion eigenvalue calculations. *Progress in Nuclear Energy* 121, 103232.
- [34] Qian, E., Kramer, B., Peherstorfer, B., Willcox, K., 2020. Lift & Learn: Physics-informed machine learning for large-scale nonlinear dynamical systems. *Physica D: Nonlinear Phenomena* 406, 132401.
- [35] Reiss, J., Schulze, P., Sesterhenn, J., Mehrmann, V., 2018. The Shifted Proper Orthogonal Decomposition: A Mode Decomposition for Multiple Transport Phenomena. *SIAM Journal on Scientific Computing* 40, A1322–A1344.
- [36] Rim, D., Moe, S., LeVeque, R.J., 2018. Transport Reversal for Model Reduction of Hyperbolic Partial Differential Equations. *SIAM/ASA Journal on Uncertainty Quantification* 6, 118–150.
- [37] San, O., Borggaard, J., 2015. Principal interval decomposition framework for POD reduced-order modeling of convective Boussinesq flows: PRINCIPAL INTERVAL DECOMPOSITION MODEL REDUCTION FRAMEWORK. *International Journal for Numerical Methods in Fluids* 78, 37–62.
- [38] Satish Balay, et. al., 2021. PETSc/TAO Users Manual ANL-21/39 - Revision 3.16.
- [39] Swischuk, R., Kramer, B., Huang, C., Willcox, K., 2020. Learning physics-based reduced-order models for a single-injector combustion process. *AIAA Journal* 58, 2658–2672. [arXiv:1908.03620](https://arxiv.org/abs/1908.03620).
- [40] Tsujita, K., Endo, T., Yamamoto, A., 2021. Fast reproduction of time-dependent diffusion calculations using the reduced order model based on the proper orthogonal and singular value decompositions. *Journal of Nuclear Science and Technology* 58, 173–183.
- [41] Udagedara, I., Helenbrook, B., Luttmann, A., Mitchell, S.E., 2015. Reduced order modeling for accelerated Monte Carlo simulations in radiation transport. *Applied Mathematics and Computation* 267, 237–251.
- [42] Volkwein, S., 2013. Proper Orthogonal Decomposition: Theory and Reduced-Order Modelling, 82.
- [43] Williams, M.O., Kevrekidis, I.G., Rowley, C.W., 2015. A Data-Driven Approximation of the Koopman Operator: Extending Dynamic Mode Decomposition. *Journal of Nonlinear Science* 25, 1307–1346.
- [44] Wirtz, D., Sorensen, D.C., Haasdonk, B., 2014. A Posteriori Error Estimation for DEIM Reduced Nonlinear Dynamical Systems. *SIAM Journal on Scientific Computing* 36, A311–A338.
- [45] Xiao, D., Fang, F., Buchan, A., Pain, C., Navon, I., Du, J., Hu, G., 2014. Non-linear model reduction for the Navier–Stokes equations using residual DEIM method. *Journal of Computational Physics* 263, 1–18.

## Appendices

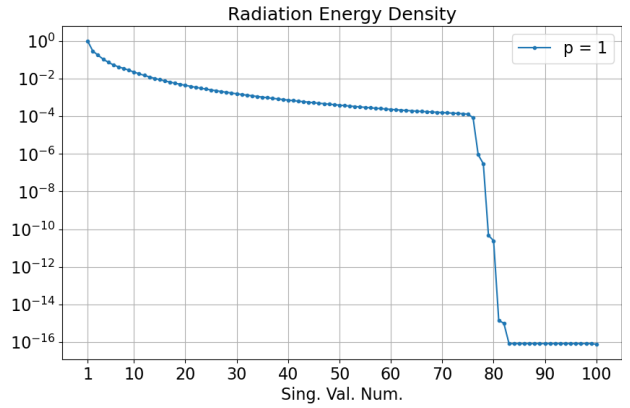
In Appendices A and B we show the relevant snapshot data, singular value decay, and DEIM-based a-priori error indicators used to determine truncations for Section 4. For plots showing the a-priori DEIM error, the shaded regions highlight the bounds of the intervals where the wave front interface begins and ends, respectively. This section is used to determine the truncations for the DEIM operators for Figures 6 and 7. Relative to its shaded counterpart, we find

that the errors indicated outside of the shaded regions have little impact on the accuracy of the ROM. For brevity, analogous plots for “PID4” and “PID8” are not shown.

**A. “PID1”**

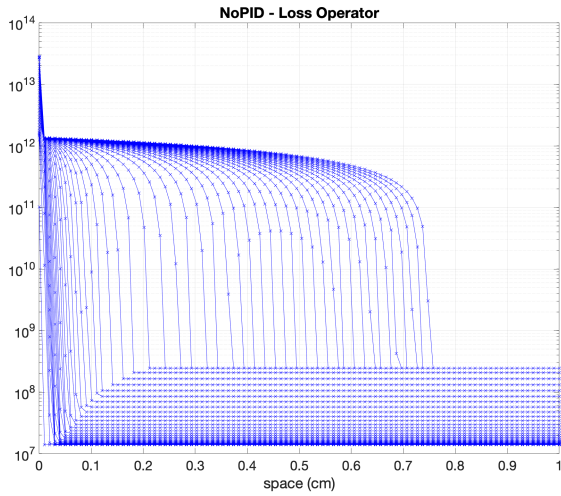


(a) Snapshots of the radiation energy density without PID.

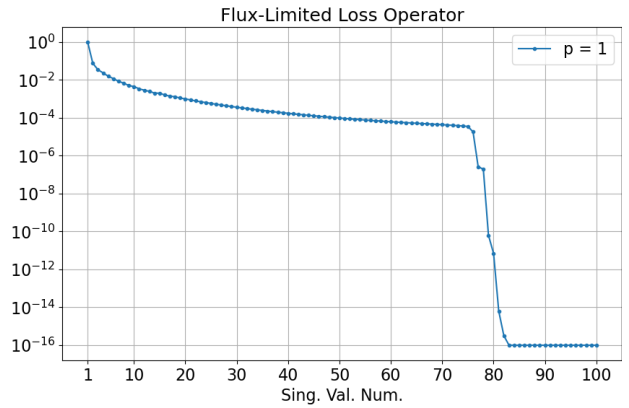


(b) Singular value decay of the radiation energy density without PID.

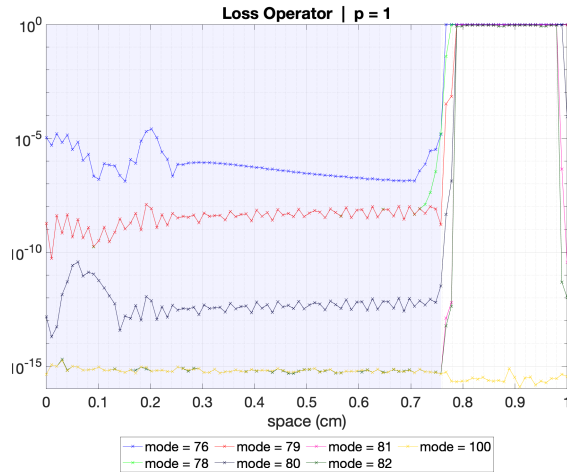
**Figure A-1:** Snapshots and associated singular value decay for the radiation energy density without PID.



(a) Snapshots of the flux-limited loss operator without PID.

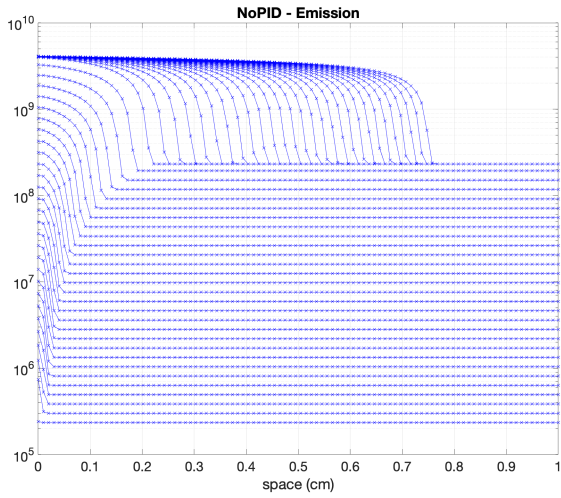


(b) Singular value decay of the flux-limited loss operator without PID.

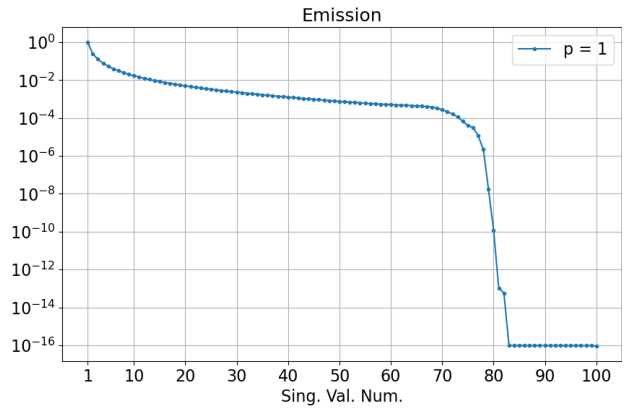


(c) A-priori error indicator for the flux limited loss operator without PID.

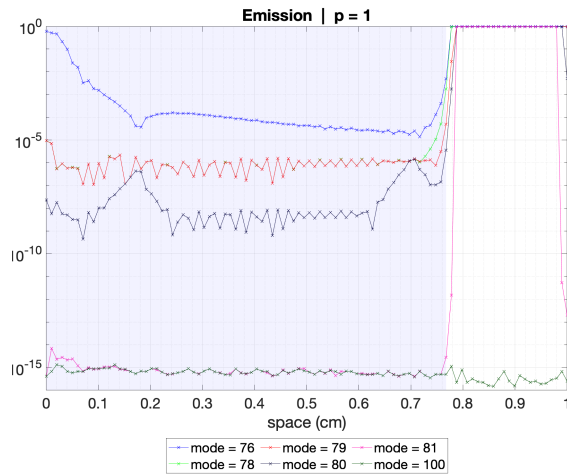
**Figure A-2:** Snapshots, singular value decay, and a-priori error indicator results for the flux-limited loss operator without PID.



(a) Snapshots of the emission source without PID.



(b) Singular value decay of the emission source without PID.

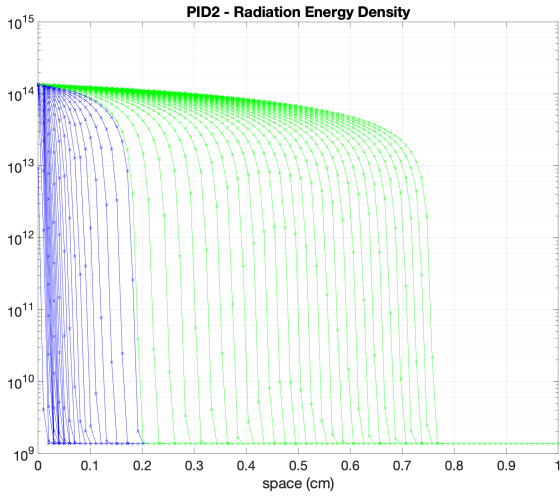


(c) A-priori error indicator for the emission source without PID.

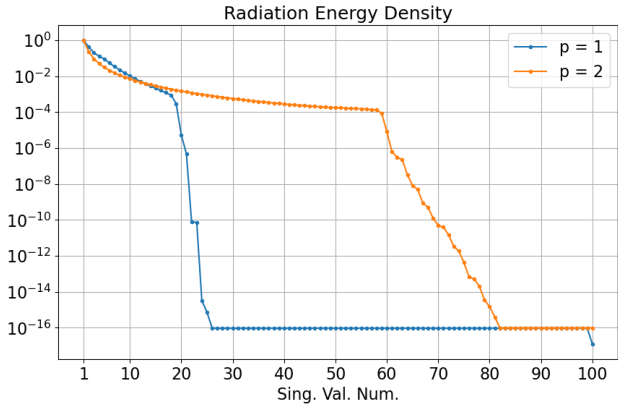
Figure A-3: Snapshots, singular value decay, and a-priori error indicator results for the emission source without PID.

## B. "PID2"

Figures A-4, A-5, and A-6 show the relevant snapshot, singular value decay, and a-priori error indicator data for the case with two PID intervals.

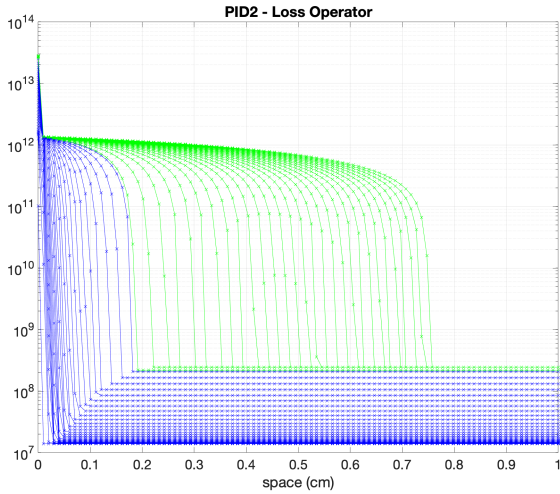


(a) Snapshots of the radiation energy density with two PID intervals.

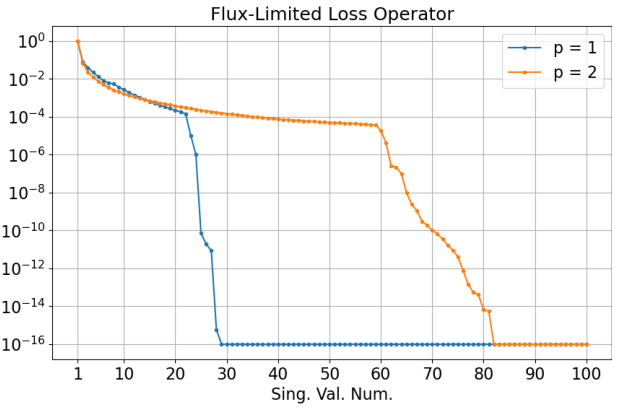


(b) Singular value decay of the radiation energy density with two PID intervals.

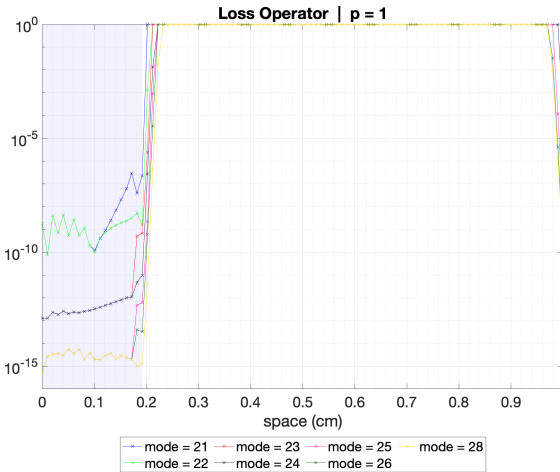
**Figure A-4:** Snapshots and associated singular value decay for the radiation energy density with two PID intervals.



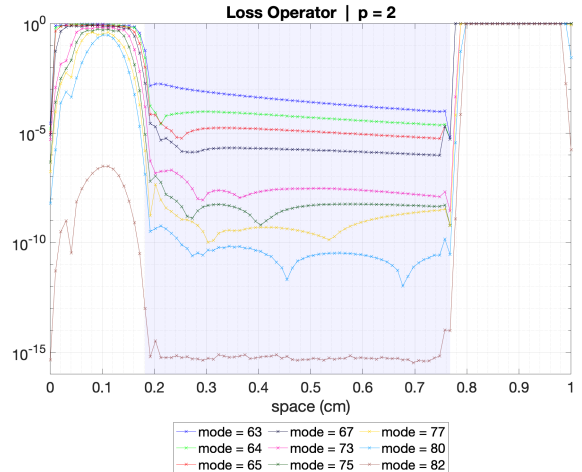
(a) Snapshots of the flux-limited loss operator with two PID intervals.



(b) Singular value decay of the flux-limited loss operator with two PID intervals.

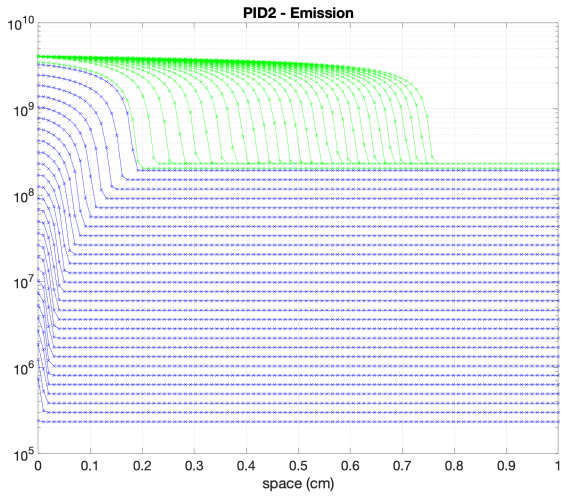


(c) A-priori error indicator for the flux-limited loss operator for interval one.

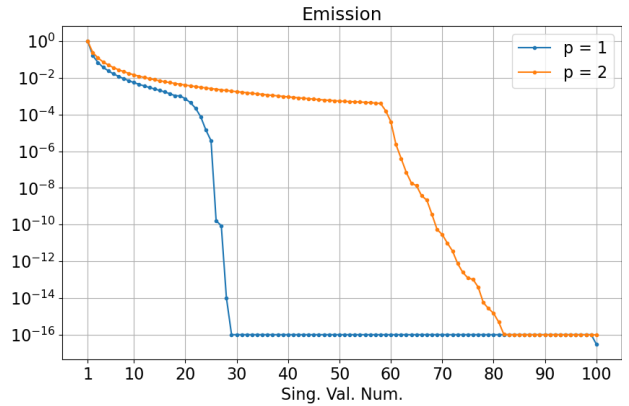


(d) A-priori error indicator for the flux-limited loss operator for interval two.

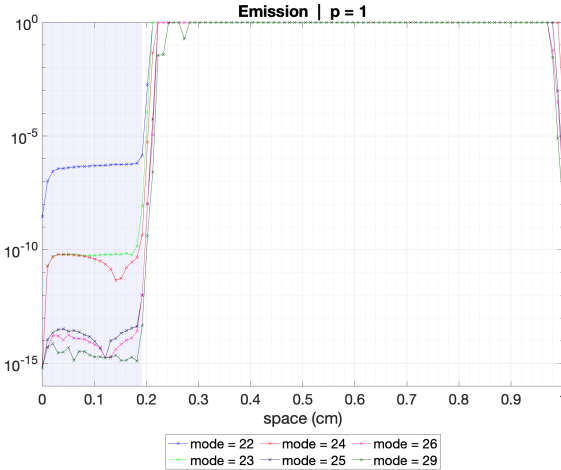
**Figure A-5:** Snapshots, singular value decay, and a-priori error indicator results for the flux-limited loss operator with two PID intervals.



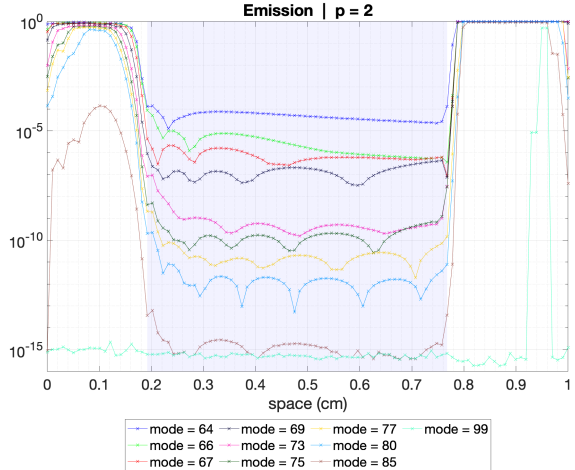
(a) Snapshots of the emission source with two PID intervals.



(b) Singular value decay of the emission source with two PID intervals.



(c) A-priori error indicator for the emission source for interval one.



(d) A-priori error indicator for the emission source for interval two.

**Figure A-6:** Snapshots, singular value decay, a-priori error indicator results for the emission source with two PID intervals.

## Highlights

### **Proper Orthogonal Decomposition Based Reduced-Order Modeling of Flux-Limited Gray Thermal Radiation**

Anthony L. Alberti, Todd S. Palmer, Camille J. Palmer

- A reduced-order modeling approach for radiation penetration problems is shown to be competitive with a full-order model in both accuracy and speed.
- The wave initialization regime is highly reducible while the reducibility of the wave propagation regime is more limited.
- When combined with slow singular value decay of advective problems and that thermal radiation penetration problems typically span many orders of magnitude, many singular modes are required.
- Nonlinear propagation of error is found to exist between the radiation energy density and flux-limited diffusion coefficient.
- Typical indicators for truncation of the radiation energy density and flux-limited loss operator are insufficient in practice due to nonlinear propagation of error.